Journal of Nonlinear Optical Physics & Materials
Vol. 9, No. 4 (2000) 423–440

DUAL FOCAL PLANE VISIBLE OPTICAL LIMITER

F. E. HERNÁNDEZ, S. S. YANG, V. DUBIKOVSKIY, W. SHENSKY III,
E. W. VAN STRYLAND* and D. J. HAGAN*,†
School of Optics/CREOL, University of Central Florida,
4000 Central Florida Blvd., Orlando, Florida 32816-2700, USA
†*E-mail: hagan@mail.creol.ucf.edu*

Received 11 August 2000

Experiments measuring the transmission of 5 nanosecond (FWHM), 532 nm pulses through an optical limiter using two different nonlinear materials at two separate focal planes show by far the highest dynamic-range measured to date. This cascaded focus, $f/5$ optical limiter combines self focusing and consequent nonlinear scattering in CS_2, with reverse saturable absorption in lead-phthalocyanine (PbPc). Both the AC Kerr effect and electrostriction contribute to the total refractive index change in CS_2. Our beam propagation code is used to model the propagation of light through the 2 cm thick CS_2 cell placed at the first focus, which protects a second 0.1 mm cell containing a solution of PbPc placed at the second focus. An aperture is placed in the focal plane of a final focusing lens to measure the "encircled" energy, defined as the energy passing through a 1.5 mrad diameter focal-plane aperture. Experiments and modeling show that the strong self-focusing in the CS_2 keeps the energy at the second cell below its damage threshold. This combination of nonlinearities clamps the maximum encircled energy below 1 μJ for input energies up to 14.5 mJ at a 10 Hz repetition rate. This corresponds to a dynamic range of at least 7500 while it is possibly much greater since no damage occurred to any device components. Here we present details of the operation of this device.

1. Introduction

In recent years, there have been considerable efforts to develop new materials and devices for high performance optical limiting. Optical limiters are devices that exhibit high transmittance for low inputs while for high inputs the transmittance is low. These devices are designed to keep the optical power, irradiance, energy or fluence transmitted below some specified maximum value, independent of the magnitude of the input. They could, for example, be used to protect sensitive detection components such as optical sensors and human eyes from damage. According to Grolier–Mazza,[1] the maximum permitted exposure (MPE) at the entrance of the human eye pupil for nanosecond pulses is 0.5 μJ/cm^2 at a wavelength of 0.5 μm.

*Also with the Department of Physics and the School of Electrical Engineering and Computer Science.

Others have determined that for nanosecond pulses permanent damage occurs for a total energy entering the eye of approximately 1 μJ.[2,3]

The performance of an optical limiter can be measured either by its figure of merit (FOM) and/or its dynamic range (DR). The FOM is defined as the ratio of linear transmittance to minimum transmittance at high energy ($T_L/T_{\min}$), while the DR is defined by the ratio of damage energy to the limiting threshold energy.[4] Because in most cases $T_{\min}$ occurs at the input energy at which the limiting device itself damages, for most limiters these two numbers are the same.

Many different nonlinear optical limiting processes, such as nonlinear refraction,[5–7] nonlinear scattering,[8–12] polarization changes,[13,14] multi-photon absorption,[15–18] and reverse saturable absorption,[19–30] have been studied in different materials including Kerr liquids, semiconductors, organics, organometallics, colloidal suspensions, and liquid crystals.[31,32]

Molecules that exhibit reverse saturable absorption (RSA) have become the subject of intense study in recent years due to their large nonlinear response. In 1967, Giuliano *et al.*,[19] were the first to describe this process determining that it occurs in materials where the excited-state absorption cross-section σ_{ex} is greater than the cross-section of the ground state σ_g. This behavior has been studied in several types of organic molecules, including metallophthalocyanines[20–24,27,28] and polymethines.[29]

For a single element of RSA material, the figure of merit (FOM), could be theoretically very large depending on the relative values of σ_{ex} and σ_g.[4] However, while an RSA material placed in a focal plane can strongly limit the transmittance of nanosecond laser pulses, the limiting element itself eventually undergoes optical damage, constraining its dynamic range (for a liquid the damage occurs to the container walls).[4] Sometimes the material still continues to limit the transmitted energy even after it has damaged.[28] However, permanent damage can be catastrophic for nonlinear liquids in glass cells and is generally undesirable for any optical limiter. To improve the performance of optical limiters using RSA, a multiple-cell device in a focused-beam geometry was developed.[4,21,23,24,30] In its simplest form, this optical device, referred to as a tandem limiter, consists of an RSA element placed at or near the focus with another element placed before the focus. Before the element near the focus damages, the one placed before focus activates, limiting the fluence or irradiance and protecting the near-focus element. Similarly, multiple RSA elements can be positioned in a converging beam geometry so as to further increase the FOM.[4] The spacing between the devices is determined by the focusing and is optimized by a specific geometrical progression as described by Hagan *et al.*[4] Experimentally, 3-element tandem limiters were shown to have FOM $\simeq$ 400.[23,24] In Ref. 24, the output energy was clamped below a maximum value of 12 μJ for input energies up to the damage energy of 7 mJ, approximately one order of magnitude better than a single-element device. This idea was extended by Miles,[30] who showed that the absolute optimum performance of an RSA limiter could be achieved by taking the limit of an infinite number of tandem elements which results in a graded molecular

concentration in the direction of focus.

Recently, we reported preliminary results of a very high dynamic range optical limiter for nanosecond pulses with a FOM $\geq$ 7500, using an $f/5$, cascaded-focus, optical geometry with a CS_2 cell in the first focal plane to protect an RSA material in the second focal plane.[33] In this paper we present a detailed experimental characterization of this optical limiter, along with a numerical beam propagation analysis that reveals how the effect of electrostriction enhances the nonlinear refraction in CS_2 for nanosecond pulses.

2. Experimental Setup

The experimental setup, shown in Fig. 1, consists of a 1 or 2 cm thick CS_2 cell at the first focus (depending on the input energy range), and an RSA solution in a thin cell (0.05–0.1 mm) at the second focus. We used a frequency-doubled, Q-switched, 5 ns Full-Width at Half-Maximum (FWHM), single-longitudinal mode Nd:YAG laser with a wavelength of 532 nm, operating at a 10 Hz repetition rate. The input beam overfills the aperture A1, to produce a nearly "flat-top" beam at the input of the system. To focus the beam into the samples we used 10 cm focal length lenses; L1 and L3. Lenses L2 ($f = 10$ cm) and L4 ($f = 4$ cm) re-collimate the beam after the first and second cells. Apertures A1 and A2 (2 cm diameter) along with A3 (0.8 cm diameter), define the $f/5$ focusing and collection geometries. In both focal planes, the low irradiance spot-size was measured via the thin-sample Z-scan technique[34] to be $\cong$ 6 μm (HW1/e^2M), which is approximately 4 times diffraction limited. A 2.5 cm diameter lens, L5, collects the whole transmitted beam into detector D1 to measure the transmitted energy. A small aperture (A4) was placed in the focal plane of L5 and in front of D1 to measure the "encircled" energy (E_{en}) which is defined as the energy passing through a 1.5 mrad diameter focal-plane aperture.[2] In our case, the focal length of L5 is 100 cm and hence the aperture diameter is 1.5 mm. A half-wave plate in combination with a polarizer was used before aperture A1 to control the total input energy. The input energy (E_i) was monitored using beamsplitter between A1 and L1 that directed a small component of the beam onto a calibrated detector. (These are not shown in Fig. 1).

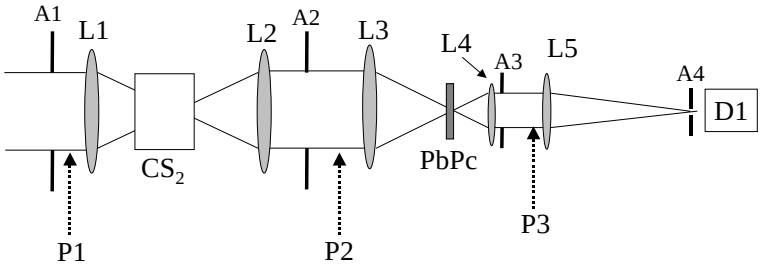

Fig. 1. Experimental setup for the, high-dynamic-range optical limiter, using an $f/5$ cascaded-focus optical geometry.

We used commercial Pb-Phthalocyanine ($PbPc(CP)_4$ 90% from Sigma–Aldrich Inc.) in chloroform solution as the RSA material.[28] This solution was filtered with a 0.22 μm filter to eliminate small particles in the solution. $PbPc(CP)_4$ has a large excited state absorption cross section associated with a long-lived (36 ns) intermolecular charge transfer state.[28] This mechanism, as well as long-term stability of the solution, requires a high concentration, so the solution must be held in very thin ($50 \sim 100$ μm) cells to maintain a sufficiently high linear transmittance, T_L.

The low irradiance transmittance for the resultant dye solution was measured at the operating wavelength of 532 nm to be 60%, while the total linear transmittance for the entire system, including Fresnel losses and the 1.5 mrad aperture, is 21% (no antireflection coatings were used on several optical surfaces). With antireflection coatings, the total linear transmittance could be as high as 60%.

3. Experimental Evaluation of the System and Discussion

To understand how the limiter works, we first identify the individual contributions of each limiting element. In Fig. 2, we show the encircled energy transmittance, (E_{en}/E_i) versus input energy (E_i) for three different experiments. The squares show the transmittance with the 1 cm CS_2 cell placed far from the first focus and the PbPc/chloroform cell positioned in the second focal plane. In this case, only the PbPc contributes to the limiting, as the irradiance in the CS_2 is too small to induce any nonlinear effect. We can see the performance of this compound as an optical limiter up to a maximum input energy of 47 μJ where the PbPc glass cell damages. This corresponds to a FOM ≈ 31. The circles show the situation where the CS_2 cell is positioned with the first focus inside the CS_2 cell (3 mm from the rear window) while the PbPc solution is moved far from the second focus. In this case,

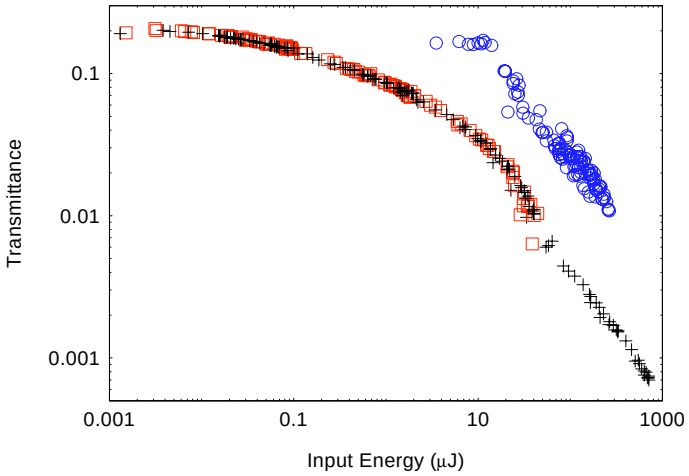

Fig. 2. Normalized encircled energy vs. input energy. Squares (□) — CS_2 cell far from the first focus and the PbPc cell at the second focus, circles (◯) — CS_2 cell at the focus and the PbPc far from the second focus, crosses (+) — Both cells are placed at their respective foci.

only the CS_2 contributes to the limiting because the fluence at the second cell is not enough to generate significant excited-state absorption. A sharp limiting threshold for the CS_2 occurs at an input of $\cong$ 14 μJ. Such a sharp threshold is expected for a self-focusing medium in which limiting is due to strong scattering from the laser-induced breakdown produced above the critical power for self focusing, P_c.[5,35] Because the CS_2 is a liquid, it is not permanently damaged by this breakdown. The crosses show the case where both cells are placed at their respective foci. The CS_2 protects the PbPc cell because P_c is reached well before the second cell damage threshold is reached. No damage is observed up to the maximum incident energy of 1 mJ for this particular set of experiments.

The dominant contribution to nonlinear refraction in CS_2 is often due to optically induced molecular reorientation, sometimes known as the AC Kerr effect. For the Kerr effect, the refractive index is given by $n(I) = n_0 + n_2 I$, and is purely irradiance dependent in a thick cell. This results in a critical *power* rather than *irradiance* since the self focusing must overcome beam spreading by diffraction. While irradiance depends on the beam area, the diffraction length (or "Rayleigh range"), z_0, is also proportional to the area. For samples much longer than z_0, the effective interaction length is $\sim z_0$, so that the beam area cancels and hence the process is power dependent. The critical power is reached when the self focusing just overcomes the diffraction.[35] Our measured value of P_c is significantly smaller than predicted from the known value of the nonlinear Kerr index in CS_2 ($n_2 = 3.1 \times 10^{-14}$ cm^2/W to yield $P_c = 8.2$ kW at 532 nm).[5] This would correspond to an energy of 43.5 μJ for our pulsewidth. However, for the tight focusing geometry and the laser pulsewidth in this experiment, the refractive index change due to electrostriction can contribute significantly to the nonlinear index change in CS_2. This is fortunate, as the Kerr effect alone is barely sufficient to protect the PbPc from damage. In Sec. 5, we describe our modeling of the contribution of electrostriction.

To better determine the dynamic range of the limiter, the experiment was repeated for higher input energies. In this experiment we used a 2 cm thick CS_2 cell, and the linear transmittance of the PbPc solution was 50%. Antireflection coatings were used on most of the optical surfaces, but the total transmittance through the entire system remained low, 21% (including the 1.5 mrad aperture). We determined that the cumulative spherical aberrations were reducing the linear transmission, particularly at the 1.5 mrad aperture. Future efforts will concentrate on improving the optical system design to minimize these aberrations. Figure 3 shows the output encircled energy as a function of input energy up to 14.5 mJ, with the second cell at two different positions. While the behavior is very good in both cases, the output energy is clamped to a lower value when the cell is positioned before the focus. As we show in Fig. 4, the two positions for the PbPc cell were determined by performing open aperture Z-scans of the thin PbPc cell.[34] These positions correspond to the Z-scan minima for this sample at low (73 nJ) and high (8.4 mJ) energies. These two positions correspond to the linear focus and 400 μm before the focus, respectively. The minimum position remains at 400 μm before focus over a wide range of input

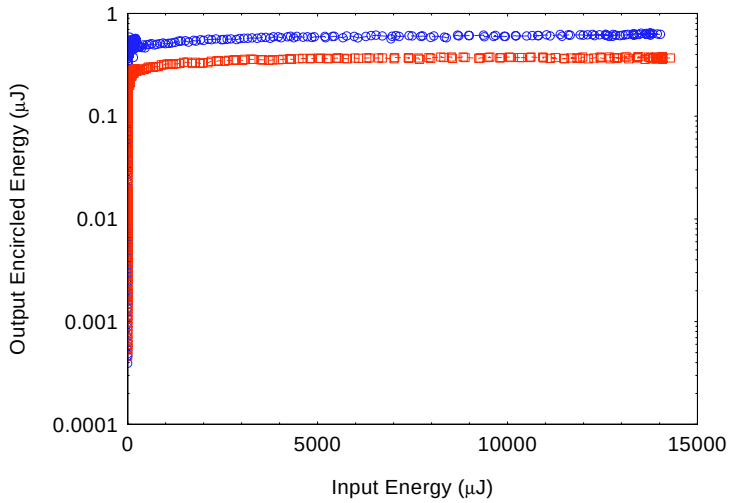

Fig. 3. Output encircled energy vs. input energy, for the high-dynamic-range optical limiter using an $f/5$, cascaded-focus optical geometry. Circles (◯) correspond to the second cell placed at the linear focus, and squares (□) to the cell positioned 400 μm before the linear focus.

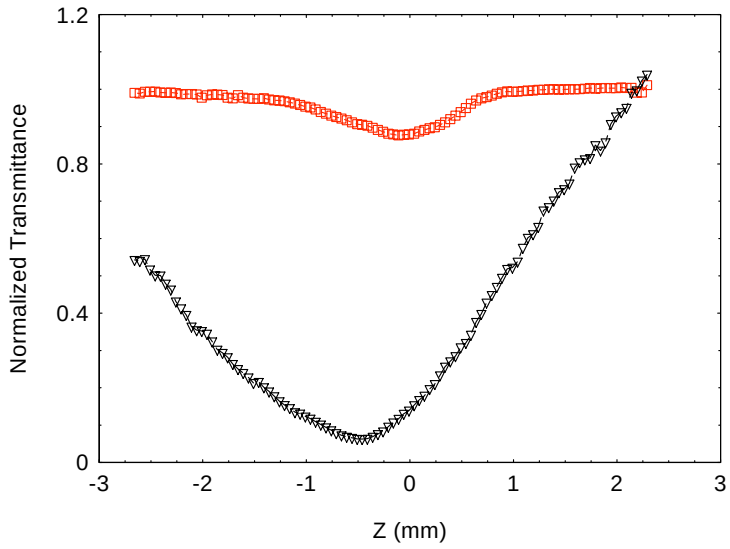

Fig. 4. Open aperture Z-scan for the PbPc/$CHCl_3$ solution at the second focus. Squares (□) — low energy $E_i = 73$ nJ, inverted triangles (▽) — high energy $E_i = 8.4$ mJ not normalized.

energies from below 1 mJ to 14.5 mJ. Evidence of degradation of the linear optical performance of the system due to aberrations is shown in Fig. 5 where data with the 1.5 mrad aperture is compared to data with the aperture removed. The effective aperture is then determined by the 1 cm diameter of detector D1. At low energy these two sets of data should coalesce since a *diffraction limited* spot would subtend substantially less than 1.5 mrad. In addition, this graph shows the effect of beam

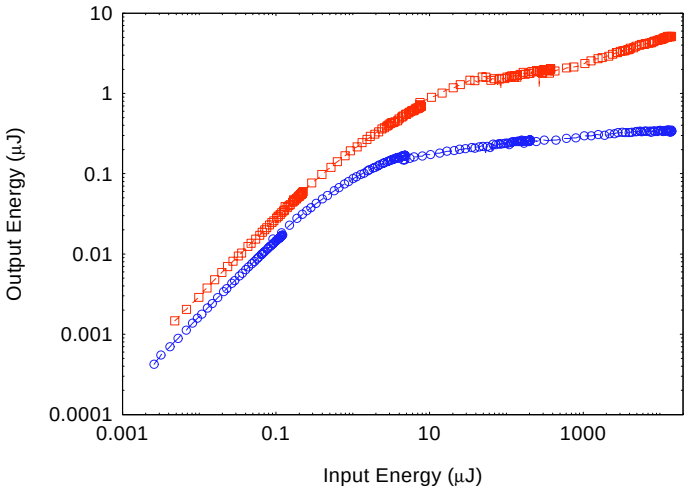

Fig. 5. Logarithmic plot of output encircled energy, circles (◯), and total transmitted energy as measured on a 1 cm diameter detector in the focal plane of lens L5, squares (□), versus incident energy.

spreading helping the limiting process. The encircled energy is clamped while the transmitted energy continues to rise slowly.

We also measured the spatial profiles of the beam for several input energies at positions P1, P2, and P3 indicated in Fig. 1. In Fig. 6, we show profiles after the first cell (P2) and after the second cell (P3). We took images at many different energies using a CCD camera with a pixel size of (12×12 μm); however, we only show beam profiles at a few representative energies, which qualitatively show all the interesting effects. At P2 we inserted a beamsplitter before the aperture to allow the beam to propagate in free space for approximately one meter. We found that this allowed us to see more changes in the beam profile with increasing input energy, as the beam profile at aperture A2 was always more or less uniform. At low input energy, 2 nJ, the beam profile at P2 [Fig. 6(a)] is indistinguishable from the input beam at P1, showing no obvious signs of spherical aberration. The spatial modulation is the spatial noise on the laser output beam profile after being expanded, clipped and propagated. However as the input is increased to 46 μJ the low spatial frequency modulation is enhanced with significant areas showing less than 50% of the maximum transmittance [see Fig. 6(b)]. As the input energy is increased to about 1 mJ and above, the pattern at P2 changes qualitatively. A fine spatial pattern evolves which changes from pulse to pulse, reminiscent of speckle, and this pattern appears to shrink to a narrow beam within the projection of the exit pupil defined by aperture A2. Figure 6(c) shows the final manifestation of this process at high energy, 6.7 mJ although the same qualitative pattern is seen from below 1 mJ up to the maximum laser output. This pattern is not seen without the increased propagation distance allowed with the beamsplitter in place. We can only speculate as to the cause of this very well defined pattern. Looking at the side of

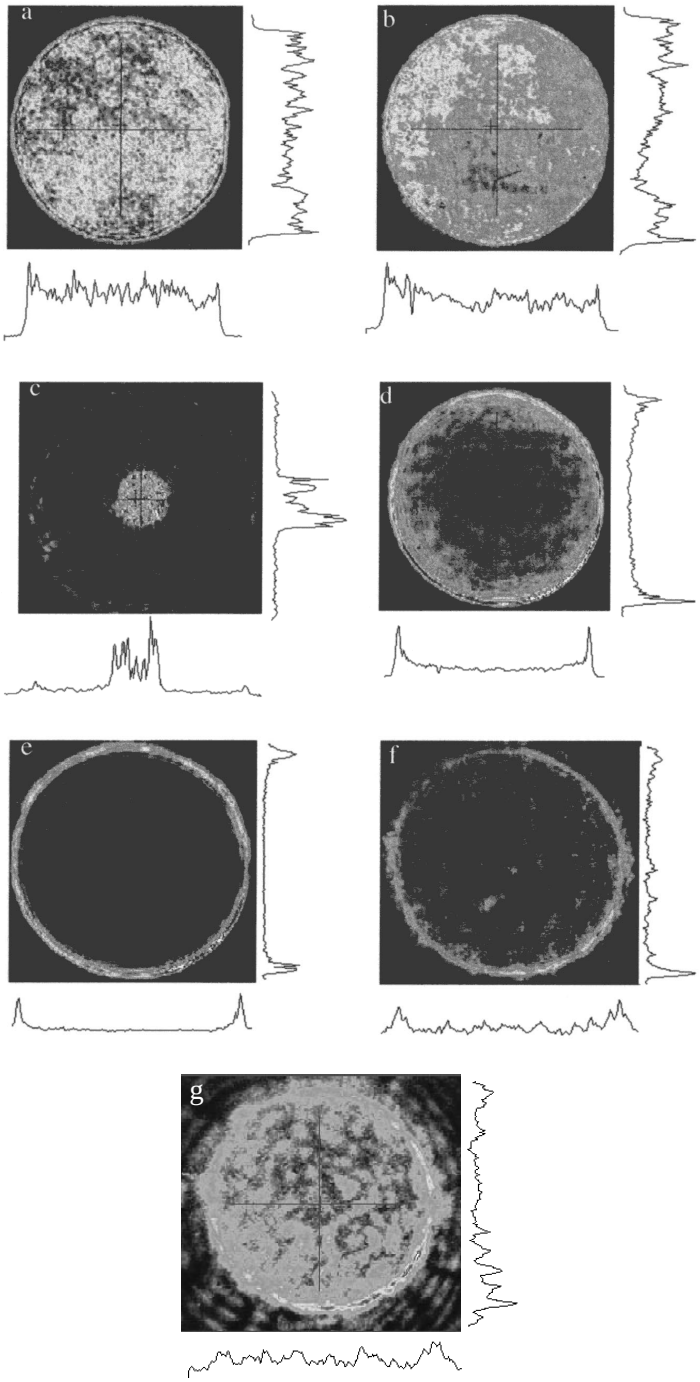

Fig. 6. Spatial beam profiles as measured on a CCD at positions P2 and P3 for several incident energies. (a) P2, 2 nJ; (b) P2, 46 μJ; (c) P2, 6.7 mJ; (d) P3, 2 nJ; (e) P3, 33 μJ; (f) P3, 2.2 mJ; (g) P3, 6.7 mJ.

the CS_2 cell, as the input energy increases a line of breakdown develops that moves closer and closer to the cell input window showing that the self focusing occurs earlier in space as well as in time, as expected. This focusing prior to the linear optics focal position means that this energy can be reimaged by lens L2 after the CS_2 cell. However, the fact that the CCD temporally integrates the entire pulse and the fact that the central beam is well defined with sharp edges means that most of the energy is contained in this stable beam. It is possible that this is related to the development of spatial solitons.[36] It seems unlikely that a temporally moving focus running back and forth as the energy increased and decreased could lead to an image with such well defined edges. In addition, it is possible that the breakdown plasma creates further lensing effects that stabilize the filamentation.[37] Modeling such beam propagation, which occurs above the threshold for ionization, is beyond the scope of this paper.

At position P3 we removed aperture A3 and also let the beam propagate for some distance (approximately 1 m). At low energy, 2 nJ, the beam appears in Fig. 6(d) as a flat top surrounded by a ring. This shows the severe spherical aberrations that accumulate with the four doublet lenses used in the system. A Zemax® simulation shows that this should not be unexpected. Images taken through the entire system appear undistorted. Unfortunately, the aberration makes full interpretation of the nonlinear propagation more difficult. As the energy increases to 33 μJ [Fig. 6(e)] the energy inside the ring appears to have been effectively eliminated while the ring remains. However, as the energy is increased further this phenomenon reverses so that the central portion of the beam, now highly modulated, fills in and the ring washes out, as shown in Fig. 6(f) for 2.2 mJ. The final figure in this series [Fig. 6(g)] at 6.7 mJ shows that energy eventually spills out beyond the extent of the original flat-top beam which would normally be clipped by aperture A3. Future studies will be performed with a lens system corrected for spherical aberration to better delineate the effects of the nonlinearities on beam propagation.

Using a fast Si photodiode, we monitored the temporal behavior of the pulse at the input, between the CS_2 and PbPc elements and at the output (positions P1, P2 and P3 in Fig. 1, respectively). In Fig. 7 we show the on-axis irradiance versus time for an input energy of 100 μJ at positions P1, P2 and P3. As expected, the effect of each nonlinear element is to limit the end of the pulse more strongly than the beginning. However, at position P2 this effect is quite small, and the peak irradiance is shifted to earlier times by only about 1 ns. As the energy corresponds to a peak power well above P_c, it might be expected that the pulse would be rapidly truncated once P_c is reached. This expectation would be reasonable if the entire beam were to undergo critical self-focusing as a unit. However, as seen in Fig. 6, our input beam profile is somewhat noisy so it is likely that the beam is breaking up into filaments as it self focuses. Further evidence for this was discussed earlier in relation to the spatial beam profiles. This should be a more gradual process than whole-beam self-focusing. At position P3, the shift of the peak is more pronounced,

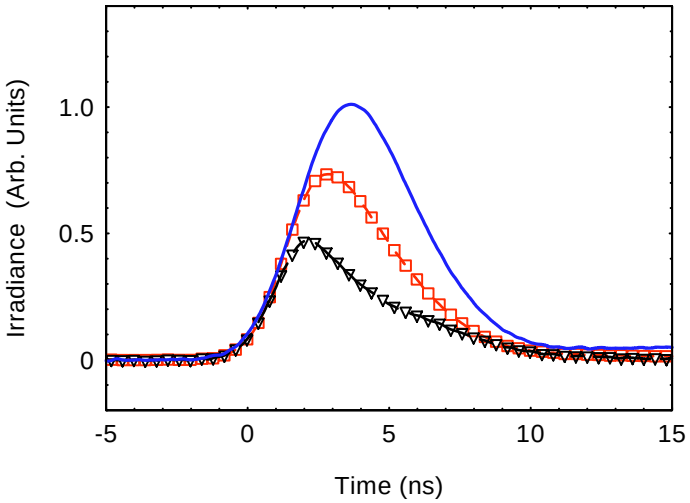

Fig. 7. Temporal behavior of the on-axis irradiance at positions P1, solid line; P2, squares (□); and P3, triangles (Δ) for an incident energy of 100 μJ.

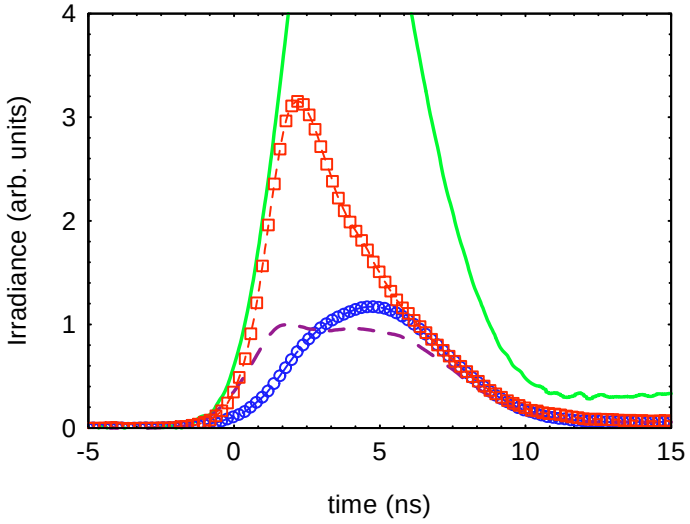

Fig. 8. Temporal behavior of the on-axis irradiance at position P3 for a incident energy of 3 mJ for three positions of the PbPc cell with respect to the high energy Z-scan of PbPc shown in Fig. 4. The dashed line is for the PbPc at the Z-scan minimum, square (□) correspond to the PbPc slightly before the Z-scan minimum and circles (◯) correspond to the PbPc sample positioned slightly after the minimum. The solid line shows the incident pulse (not to scale) for reference.

as would be expected since the PbPc dominates the low energy limiting and the limiting increases with time as the excited state population builds up.

At higher energy, the temporal behavior at P3 provides some insight as to how the CS_2 affects the position of the second focus. Figure 8 shows the temporal behavior of the on-axis irradiance at a 3 mJ input energy for three positions of the

PbPc with respect to the Z-scan minimum at this energy, (i.e. high energy Z-scan as shown in Fig. 4.) The input pulse (solid line) is also shown for reference. With the PbPc placed after (circles) the Z-scan minimum, the transmitted pulse is more strongly attenuated for early times than for other positions of the PbPc. This is probably because at early times, the self-focusing in the CS_2 is weak, so that the second beam waist is still close to its linear optics position. Hence early in the pulse, the RSA should be stronger with the PbPc placed closer to the low-energy Z-scan minimum. For the PbPc placed before the high energy Z-scan minimum, (squares) the beam waist starts out far from the sample so the RSA is weak at early times. With the PbPc placed at minimum transmittance, (dashed line) the overall peak is reduced and the pulse is slightly temporally modulated. For early times the limiting is somewhat less than optimal, but for later times the limiting efficiency increases.

4. Damage Testing

In order to test the ultimate effectiveness of this limiter design for protecting detectors against nanosecond, 532 pulses, we placed a commercial video camera (JVC model # GR-AX750U) in place of the final focusing lens. Unfortunately, due to an automatic-iris exposure control, the exact $f/\#$ could not easily be determined. When subjected to single pulses separated by seconds no apparent damage was observed up to the maximum laser output (14.5 mJ). The appearance of the monitor showed bright flashes that progressively bloomed as the input was increased; however, they never covered the entire field of view and only lasted for a couple of frames. On the other hand, when the laser beam was allowed to enter the camera at the full 10 Hz repetition rate, a single-pixel damage site was observed at an input of $\cong$ 1 mJ. After a second or two and at higher inputs (a few mJ) this single site grew into multiple pixels that then progressively turned into a black line in the scan (only in one direction from the original damage site). Apparently the effects of a single pulse on the temperature or CCD readout current lasts for more than 1/10th of a second so that the accumulated heat or current causes permanent damage. It also remains to be seen what the effect of reducing the spherical aberrations in the optical system will have on the operation of the device.

5. Numerical Modeling

Beam propagation codes have been successfully used to model propagation of light in bulk nonlinear media. The finite-difference Crank–Nicholson algorithm, which proved to be more efficient than spectral techniques in terms of computational speed and stability, is used here as a tool for numerical analysis.[38,39] The reasonable assumption of cylindrical symmetry is made to reduce the dimensionality of the problem and decrease computational time. Here we make a comparative analysis of the contributions of the Kerr effect and electrostriction to critical self-focusing for different pulsewidths assuming Gaussian temporal and spatial profiles. The results

qualitatively explain the experimentally observed reduction of the critical power for self-focusing, P_c.

Using a nonlinear optical beam propagation code previously developed for optical limiting,[38,39] we have modeled the beam propagation through CS_2 including both Kerr effect and electrostriction for a variety of different pulsewidth and beam radius combinations. Molecular reorientation in CS_2 ($\cong$ 2 ps response time) can be considered to be instantaneous on the time scale of the experiment.[5] Therefore, the calculation of the Kerr effect contribution is relatively straightforward. Local changes in the refractive index are found as follows:

$$\Delta n(r,z) = n_2 I(r,z)\,, \tag{1}$$

where n_2 is the Kerr index and $I(r,z)$ is the irradiance distribution. When n_2 is positive, self-focusing results. For samples that are thicker than the Rayleigh range, as self focusing results in an increase in irradiance, which in turn leads to more self focusing, and so on, there is a sharp threshold above which the beam will collapse to a very small size, resulting in breakdown of the material. According to Marburger,[40] the threshold occurs at a critical power, P_c, irrespective of the way the beam is focused into the sample. For a pure Kerr-like nonlinearity:

$$P_{cr} = \frac{3.77\lambda^2}{8\pi n n_2}\,, \tag{2}$$

where λ is the wavelength of light and n is the linear refractive index. Our numerical model of beam propagation is adequate for irradiance levels up to values close to P_c. However, it cannot completely describe critical self-focusing. In the later stages of beam collapse the paraxial approximation, which is used in the Crank–Nicholson algorithm, is no longer valid, and the full vectorial Maxwell equations should be solved to determine the subsequent evolution of the optical field.[41,42] Also our analysis here does not aim to adequately describe light scattering resulting from plasma and bubble formation in the liquid as the optical field increases above P_c. Hence, we concentrate on modeling the relative contributions from the Kerr effect and electrostriction to the nonlinear refraction just below the critical power.

Changes of the refractive index due to electrostriction are not local. The increased density and hence refractive index result from the transport of liquid towards the focal region. Therefore, the effect is only important when the pulse width is comparable to or larger than the transit time of acoustic waves across the beam. The density changes can be described by the linearized hydrodynamic equations. For a non-viscous liquid, we can combine the continuity and Navier–Stokes equations to obtain the acoustic equation for a density perturbation $\Delta\rho$:[38]

$$\frac{\partial}{\partial t}\left[\frac{\partial^2(\Delta\rho)}{\partial t^2} - C_S^2\nabla^2(\Delta\rho)\right] = \frac{C_S^2\beta}{c_p}\,\nabla^2(\alpha_L I) - \frac{\gamma^e}{2nc}\frac{\partial}{\partial t}\,\nabla^2 I\,. \tag{3}$$

Here the terms on the right-hand side represent absorption (with consequent thermal expansion) and electrostriction respectively, β is the thermal expansion coefficient,

c_p is the specific heat, α_L is the linear transmittance, c is the speed of light, C_S is the speed of sound, and $\gamma^e = (n^2-1)(n^2+2)/3$ is the electrostrictive coupling constant derived from the Lorentz-Lorenz law.

Since absorption is negligible at 532 nm in CS_2, the first term on the right hand side can be dropped. Using the relation $(\partial n/\partial\rho)_T = \gamma^e/(2n\rho)$, we end up with the following equation for the index change:

$$\frac{\partial^2(\Delta n)}{\partial t^2} - C_S^2\nabla^2(\Delta n) = -\left(\frac{\gamma^e}{2n}\right)^2 \frac{1}{c\rho}\nabla^2 I\,. \tag{4}$$

This equation is solved numerically for each time-slice of the optical pulse and the results are stored as the initial index distribution for the next time-slice. In this way the optical pulse and acoustic wave propagation are treated simultaneously.

Contributions of electrostriction and the Kerr effect to the refractive index change are shown for the temporal center of the pulse on the axis of the beam in Fig. 9. The 14 μJ incident energy is just below P_c. For our experimental conditions of 5 ns (FWHM) pulses and 6 μm (HW1/e^2M) beam radius, the refractive index change due to electrostriction is approximately equal to that due to molecular reorientation in the center of the pulse. When both effects are considered, the change in refractive index is larger than the linear sum of the corresponding index changes. This happens due to the nonlinear character of beam propagation. The additional effect of index change due to electrostriction contributes to the increase of irradiance, which in turn results in larger nonlinear index change due to Kerr

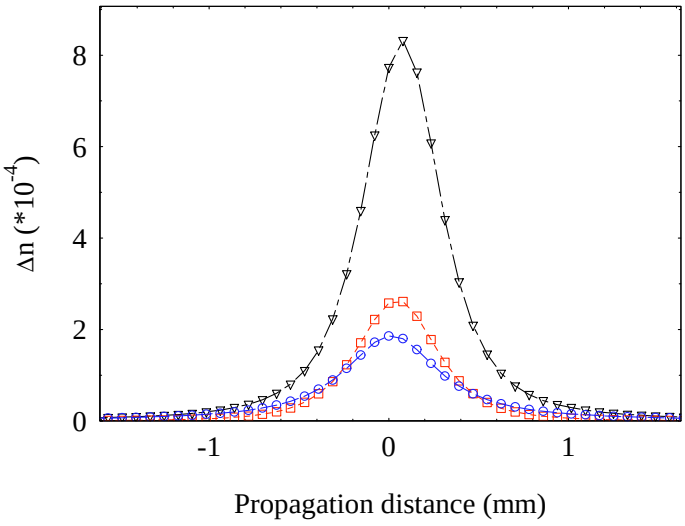

Fig. 9. Calculation of the on-axis refractive index changes versus position in a CS_2 cell at the center of the pulse in time. Input energy, 14 μJ, beam waist $w_0 = 6$ μm, pulsewidth $\tau_{\mathrm{FWHM}} = 5$ ns. Circles (◯) — pure Kerr, squares (□) — pure electrostriction, inverted triangles (∇) — both effects at the same time.

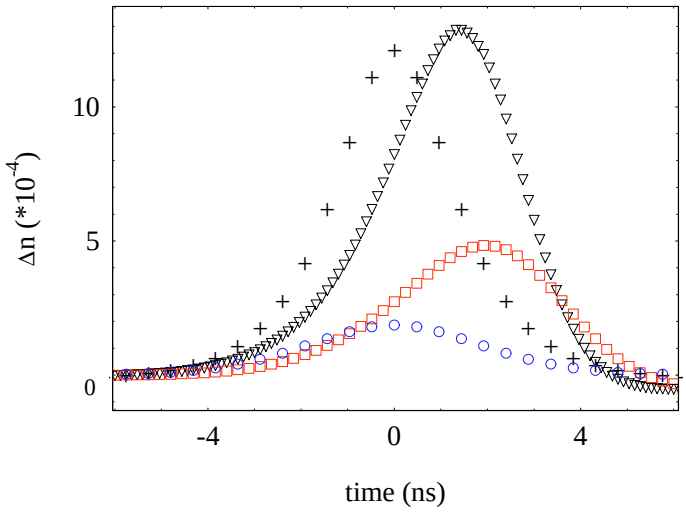

Fig. 10. Calculation of the on-axis refractive index changes versus time, within the pulse. E_i = 14 μJ, beam radius $w_0 = 6$ μm, pulse width $\tau_{\mathrm{FWHM}} = 5$ ns. Circles (◯) — pure Kerr, squares (□) — pure electrostriction, inverted triangle (∇) — both effects at the same time, crosses (+) — pure Kerr for $E = 2.5\ E_i$.

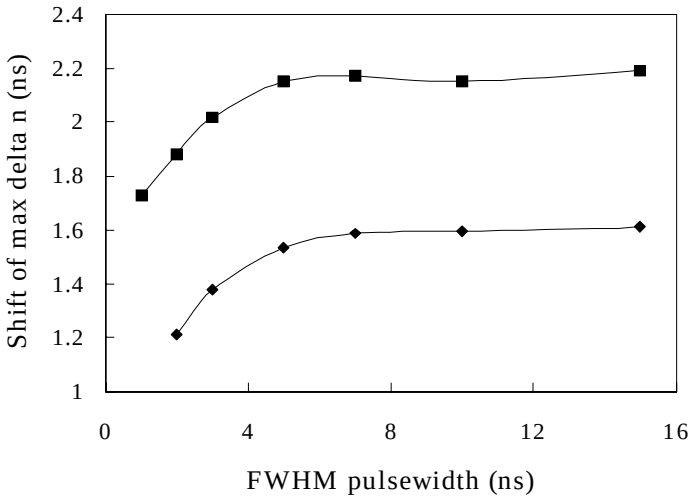

Fig. 11. Shift of the maximum refractive index change vs. pulse width. Constant power and beam radius $w_0 = 6$ μm (HW1/e^2M). Squares (■) — Electrostriction only, diamonds (♦) — both Kerr effect and electrostriction. Note: lines are to guide the eyes and are not the results of actual calculations.

effect, and vice versa. In this way, both effects enhance each other in the process of propagation. This explains why the critical power for self-focusing is considerably lower than the value obtained from Eq. (2). As shown in Fig. 10, the refractive index change due to the Kerr effect reaches its maximum in the middle of the pulse. The electrostrictive contribution to the refractive index, however, continues to increase

and is maximized some time, τ, after the center of the pulse has passed. This delay time τ is related to the time it takes for the density perturbations to move across the beam waist (at the speed of sound). It also depends on pulse duration as shown in Fig. 11. A similar, but smaller shift of the maximum refractive index change occurs when both Kerr effect and electrostriction are taken into account. For our experimental parameters, the refractive index change exceeds that of the pure Kerr effect by a factor of 4 in the center of the pulse, where the incident irradiance is maximum, and the peak index change due to the combined effects is 6.5 times the maximum index change due to the Kerr effect alone. Though the mechanisms of index changes due to electrostriction and Kerr effect are different, we can gain some insight into the self-focusing process by comparing the values of the maximum refractive index change due to both processes with that of the pure Kerr effect at higher power levels. The resulting index change is comparable to that induced by the pure Kerr effect when the pulse energy is $\cong 2.5$ times higher (crosses in Fig. 10). This agrees reasonably with the experimentally observed factor of $\cong 3$ difference with respect to P_c calculated from Eq. (2) and explains the experimentally observed critical power of 2.6 kW. The difference between experimental results and numerical simulation may be attributed to combination of experimental error, the assumption of a Gaussian spatial profile and the use of the paraxial approximation, which does not hold when critical self-focusing occurs in nonlinear media. A more rigorous numerical treatment, however, results in a substantial increase of calculation time and therefore has not been attempted at this point.

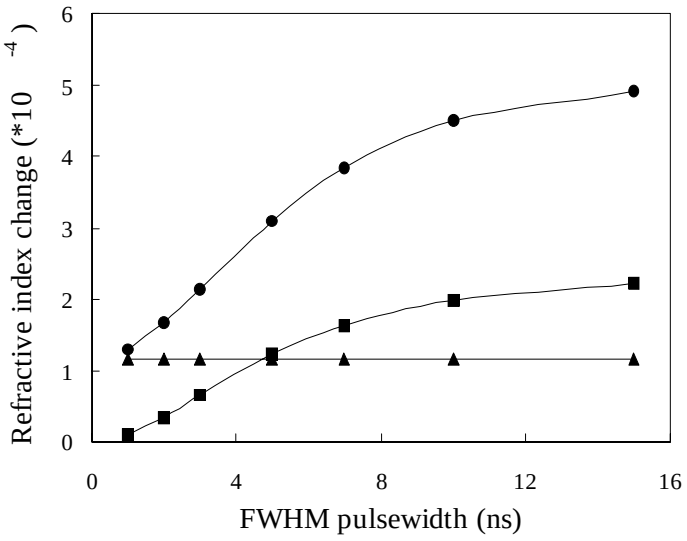

Fig. 12. Calculated on axis refractive index change at maximum irradiance as a function of pulse width for constant power and 6 μm beam radius. Triangles (▲) — Kerr effect only, squares (■) — electrostriction only, circles (•) — both effects at the same time. Note: lines are to guide the eyes and are not the results of actual calculations.

For a constant focused spot size, electrostriction should provide lower critical powers for longer pulses which allow the density changes to propagate farther within the pulse.[38] In Fig. 12, we show the refractive index change at pulse center versus pulse width, for constant power and beam waist (6 μm HW1/e^2M). For a pure Kerr effect the refractive index change does not depend on pulse width while the electrostrictive contribution increases for longer pulses, as expected. When both effects are included at the same time, the index changes behave as in the case of pure electrostriction. Therefore, P_c should decrease as the pulsewidth increases. However, the energy at which P_c is obtained will still increase as the pulse width increases simply because the energy increases linearly with pulse width. This rate of increase is less for electrostriction than for the Kerr effect.

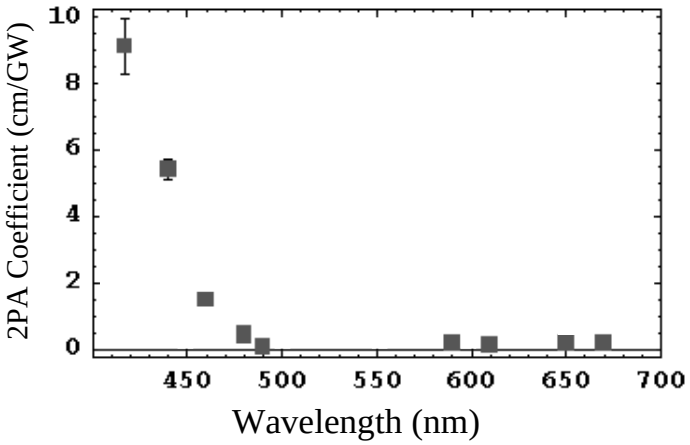

Fig. 13. Measured two photon absorption coefficient versus incident wavelength for CS_2. (After Ref. 43.)

6. Conclusions

The multiple focus geometry (here 2 foci) of the optical limiter reported here adds to the flexibility in optimizing the use of materials' nonlinear optical responses. While we have demonstrated an optical limiter with a dynamic range of the order of 10^4 using CS_2 and PbPc, there are a variety of other options to try that might not be possible with other limiter geometries. For example, CS_2 might be replaced by a carbon black suspension (CBS) which can have fairly high linear transmittance and has been shown to give excellent, broadband limiting with a slightly higher limited output. CBS has also been shown to limit for longer pulses, where it is expected that the CS_2 may no longer work well. Even though the electrostrictive contribution to the index change grows for longer pulses, the energy transmitted by the CS_2 will rise for longer pulses. It is not yet clear whether it will continue to protect the PbPc cell for 100 ns or longer pulses. Another option is use CS_2 as the host for CBS, thus combining their nonlinearities. It may also be possible to add two-

photon absorber (2PA) dyes into the first cell (perhaps using CS_2 as the solvent). Again, the linear loss can be held negligible. Also many 2PA dyes exhibit excited state absorption which can substantially increase their limiting performance.[17] 2PA dyes have shown promise but have not been able to limit the output to low enough levels. However, the combination of 2PA with the second RSA cell may work well. As it turns out, CS_2 exhibits 2PA for wavelengths shorter than 490 nm as seen in Fig. 13.[43] Such processes may also extend the wavelength coverage of limiting devices. PbPc exhibits RSA from 440 nm to 610 nm;[44] however, the linear absorption is large outside this bandwidth, providing protection. Clearly, the use of two focal planes offers a number of new possibilities for the optimization of optical limiting.

Acknowledgments

We gratefully acknowledge the support of the National Science Foundation (grant ECS# 9970078), the Office of Naval Research (grant number N00014-97-1-0936) and the Naval Air Warfare Center Joint Service Agile Program, contract number N00421-98-C-1327). We would like to acknowledge Dr. Deveaux Fabrice (Groupe d'ONL Laboratoire P.M. Duffieux, UFC, Besancon, France) for image acquisition suggestions.

References

1. V. Grolier-Mazza, *Nonlin. Opt.* **21**, 73 (1999).
2. R. C. Hollins, SPIE **3282**, 2 (1998).
3. D. H. Sliney, *Nonlin. Opt.* **21**, 1 (1999).
4. D. J. Hagan, T. Xia, A. A. Said, T. H. Wei and E. W. Van Stryland, *Int. J. Nonlin. Opt. Phys.* **2**, 483 (1993).
5. M. J. Solieau, W. E. Williams and E. W. Van Stryland, *IEEE J. Quantum Electron.* **QE-19**, 731 (1983).
6. R. C. Leite, S. P. S. Porto and T. C. Damen, *Appl. Phys. Lett.* **10**, 100 (1967).
7. E. W. Van Stryland, Y. Y. Wu, D. J. Hagan, M. J. Solieau and K. Mansour, *JOSA* **B5**, 1980 (1988).
8. K. Mansour, E. W. Van Stryland and M. J. Soileau, *SPIE* **1105**, 91 (1989).
9. X. Sun, R. Q. Yu, G. Q. Xu, T. S. A. Hor and W. Ji, *Appl. Phys. Lett.* **73**, 3632 (1998).
10. T. Xia, A. Dogariu, K. Mansour, D. J. Hagan, A. A. Said, E. W. Van Stryland and S. Shi, *J. Opt. Soc. Am.* **B15**, 1497 (1998).
11. L. Vivien, E. Anglaret, D. Riehl and F. Hache, *Opt. Commun.* **174**, 271 (2000).
12. X. Sun, Y. Xiong, P. Chen, J. Lin, W. Ji, J. H. Lim, S. S. Yang, D. J. Hagan and E. W. Van Stryland, *Appl. Opt.* **39**, 1998 (2000).
13. G. E. Dovgalenko, M. Klotz, G. Salamo and G. L. Wood, *Appl. Phys. Lett.* **68**, 287 (1996).
14. F. E. Hernández, S. Yang, D. Hagan and E. W. Van Stryland, *Mol. Cryst. Liq. Cryst.* in press (2000).
15. J. L. Bredas, T. Kogej, D. Belgonne and S. R. Marder, *Nonlin. Opt.* **298**, 1 (1999).
16. G. S. He, J. D. Bhawalkar, P. N. Prasad and B. A. Reinhard, *Opt. Lett.* **20**, 1524 (1995).
17. A. A. Said, C. Wamsley, D. J. Hagan, E. W. Van Stryland, B. A. Reinhardt, P. Roderer

and A. G. Dillard, *Chem. Phys. Lett.* **228**, 646 (1994).
18. G. S. He, R. Gvishi, P. N. Prasad and B. A. Reinhardt, *Opt. Commun.* **117**, 133 (1995).
19. C. R. Giuliano and L. D. Hess, *IEEE J. Quantum Electron.* **QE-3**, 358 (1967).
20. T. H. Wei, D. J. Hagan, M. J. Sence, E. W. V. Stryland, J. W. Perry and D. R. Coulter, *Appl. Phys.* **B54**, 46 (1992).
21. T. Xia, D. J. Hagan, A. Dogariu, A. A. Said and E. W. Van Stryland, *Appl. Opt.* **36**, 4110 (1997).
22. J. W. Perry, in "Nonlinear optics of organics molecules and polymers", CRC Press, eds. H. S. Nalwa and S. Miyata (Boca Raton, FL, 1997), pp. 813–840.
23. A. A. Said, T. Xia, D. J. Hagan, A. Wajsgrus, S. Yang, D. Kovsh and E. W. Van Stryland, Conf. on Nonlinear Optical Liquids, *Proc. SPIE.* **2853**, (1996).
24. J. W. Perry, K. Mansour, J. Y. S. Lee, X. L. Xu, P. V. Bedwhorth, C. T. Chen, D. Ng, S. R. Marder, P. Miles, T. Wada and H. Sasaba, *Science* **273**, 1533 (1996).
25. K. J. McEwan, J. M. Robertson, H. L. Anderson, *MRS Symposium Proceedings Series* **479**, (1997).
26. D. G. Mclean, R. L. Sutherland, M. C. Brant, D. M. Brandelik, P. A. Fleitz and T. Pottenger, *Opt. Lett.* **18**, 239 (1993).
27. A. Kobyakov, D. J. Hagan and E. W. Van Stryland, *J. Opt. Soc. Am.* **B17**, 1884 (2000).
28. J. S. Shirk, R. G. S. Pong, F. J. Bartoli and A. W. Snow, *Appl. Phys. Lett.* **63**, 1880 (1993).
29. J. H. Lim, O. V. Przhonska, S. Khodja, S. Yang, T. S. Ross, D. J. Hagan, E. W. Van Stryland, M. V. Bondar and Y. L. Shominsky, *Chem. Phys.* **245**, 79 (1999).
30. P. Miles, *Appl. Opt.* **33**, 6965 (1994).
31. I. C. Khoo, M. V. Wood, B. D. Guenthen, M. Y. Shih, P. H. Chen, Z. Chen and X. Zhang, *Opt. Exp.* **2**, pp. 471–482 (1998); I. C. Khoo *et al.*, *Opt. Exp.* **4**, pp. 431–442 (1999).
32. V. V. Danilov, A. G. Kalintsev, N. V. Kamanian and S. A. Tul'skit, *Tech. Phys. Lett.* **24**, 359 (1998).
33. F. E. Hernández, S. Yang, E. W. Van Stryland and D. J. Hagan, *Opt. Lett.* **25**, 1180 (2000).
34. M. Sheik-Bahae, A. A. Said, T. H. Wei, D. J. Hagan and E. W. Van Stryland, *IEEE J. Quantum Electron.* **26**, 760 (1990).
35. R. W. Boyd, *Nonlin. Opt.* **257** (Academic Press, San Diego, 1992).
36. G. I. Stegeman, University of Central Florida, private communication (2000).
37. M. Mlejnek, E. M. Wright and J. V. Moloney, *Opt. Lett.* **23**, 382 (1998).
38. D. Kovsh, D. J. Hagan and E. W. Van Stryland, *Opt. Exp.* **4**, 315 (1999).
39. D. Kovsh, S. Yang, D. J. Hagan and E. W. Van Stryland, *Appl. Opt.* **38**, 5168 (1999).
40. J. H. Marburger, *Prog. Quantum Electron.* **4**, 35 (1975).
41. S. Chi and Q. Guo, *Opt. Lett.* **20**, 1598 (1995).
42. R. de la Fuente, O. Varela and H. Michinel, *Opt. Commun.* **173**, 403 (2000).
43. T. S. Ross, Ph.D. Dissertation, University of Central Florida (1998).
44. J. S. Shirk, R. G. S. Pong, S. R. Flom, F. J. Bartoli, M. E. Boyle and A. W. Snow, *Pure Appl. Opt.* **5**, 701 (1996).